ADVANCED MATERIALS
www.advmat.de

Ternary Ta_2PdS_6 Atomic Layers for an Ultrahigh Broadband Photoresponsive Phototransistor

Peng Yu, Qingsheng Zeng, Chao Zhu, Liujiang Zhou, Weina Zhao, Jinchao Tong, Zheng Liu,* and Guowei Yang*

2D noble-transition-metal chalcogenides (NTMCs) are emerging as a promising class of optoelectronic materials due to ultrahigh air stability, large bandgap tunability, and high photoresponse. Here, a new set of 2D NTMC: Ta_2PdS_6 atomic layers is developed, displaying the excellent comprehensive optoelectronic performance with an ultrahigh photoresponsivity of 1.42×10^6 A W^{-1}, detectivity of 7.1×10^{10} Jones and a high photoconductive gain of 2.7×10^6 under laser illumination at a wavelength of 633 nm with a power of 0.025 W m^{-2}, which is ascribed to a photogating effect via study of the device band profiles. Especially, few-layer Ta_2PdS_6 exhibits a good broadband photoresponse, ranging from 450 nm in the ultraviolet region to 1450 nm in the shortwave infrared (SIR) region. Moreover, this material also delivers an impressive electronic performance with electron mobility of ≈25 $cm^2V^{-1}s^{-1}$, I_{on}/I_{off} ratio of 10^6, and a one-year air stability, which is better than those of most reported 2D materials. Our studies underscore Ta_2PdS_6 as a promising 2D material for nano-electronic and nano-optoelectronic applications.

Recently, 2D noble-transition-metal chalcogenides (NTMCs) are attracting enormous attention due to their fascinating properties,[1] including widely tunable bandgap,[2–4] ultrahigh air stability,[5,6] structural anisotropy,[6–9] and moderate carrier mobility.[1,6,10–12] They can be applied to various fields including electronics,[1–6,9,10,12–16] optoelectronics,[6–8,11] sensors,[8,17] and catalysis.[18,19] Compared to most common 2D transition-metal dichalcogenides (TMDs),[20,21] NTMCs have wide layer-dependent bandgap variations and strong interlayer interactions due to the existence of the strong d^2sp^3 hybridizations between group-10 noble elements and chalcogen atoms. Such a wide layer-dependent bandgap for NTMCs enables NTMC-based photodetectors with detection ranging from the visible to near-infrared (NIR) and mid-infrared (MIR) regions, for example, bilayer $PtSe_2$-based photodetector with detection ranging from the visible to MIR (10 µm),[11] 10.6 µm $PdSe_2$-based phototransistor.[8] In addition, strong d^2sp^3 hybridizations and the resulting strong covalent intralayer interactions enable NTMCs nanoflakes to deliver high air stabilities compared to other 2D materials, for example, a $PtSe_2$-based field-effect transistor (FET) exposed to air varies little with time.[5] Ultrahigh air stability, combined with relatively high carrier mobility and on/off ratio, also make NTMCs promising channel materials for FETs with the prospect of practical applications. Interestingly, palladium-based NTMCs possess a unique puckered pentagonal structure composed of PdS_4 or $PdSe_4$ quadrilaterals linked to each other by S or Se atoms to form a 2D layer, leading to an anisotropic planar orthogonal construction feature. This is in contrast to the isotropic planar hexagonal structure of most 2D materials, and may enable the development of anisotropic phototransistors based on palladium-based NTMCs.[10,12] Currently, 2D NTMCs have become a shining star in the 2D family, stimulating us to discover new NTMC members as well as new physical and chemical effects.

Until now, only a few 2D NTMCs were reported, that is, PtQ_2 (Q = S, Se, Te),[1,11,14] PdQ_2 (Q = Se, Te),[7,10,15] Pd_2Se_3,[22] $Pd_3P_2S_8$,[19] which is far from sufficient to meet the growing demand for high-air-stable 2D materials. Among these NTMCs, we developed five materials covering PtS_2,[1] $PtSe_2$,[11] $PdSe_2$,[10,12] Pd_2Se_3,[22] and $Pd_3P_2S_8$,[19] in which 2D PtS_2 nanoflakes were

Dr. P. Yu, Prof. G. Yang
State Key Laboratory of Optoelectronic Materials and Technologies
School of Materials Science and Engineering
Sun Yat-sen University
Guangzhou 510275, P.R. China
E-mail: yupeng9@mail.sysu.edu.cn
Dr. Q. Zeng, Dr. C. Zhu, Prof. Z. Liu
School of Materials Science and Engineering
Nanyang Technological University
50 Nanyang Avenue, Singapore 639798, Singapore
E-mail: z.liu@ntu.edu.sg
Prof. L. Zhou
Institute of Fundamental and Frontier Sciences
University of Electronic Science and Technology of China
Chengdu 610054, P.R. China
Dr. W. Zhao
Guangdong Key Laboratory of Environmental Catalysis and Health Risk Control
School of Environmental Science and Engineering
Institute of Environmental Health and Pollution Control
Guangdong University of Technology
Guangzhou 510006, P.R. China
Dr. J. Tong
School of Electrical and Electronic Engineering
Nanyang Technological University
50 Nanyang Avenue, Singapore 639798, Singapore
The ORCID identification number(s) for the author(s) of this article can be found under https://doi.org/10.1002/adma.202005607.

DOI: 10.1002/adma.202005607

prepared via chemical vapor transport (CVT) method and the following mechanical exfoliation method in May 2014, which may, to the best of our knowledge, be the earliest record with respect to 2D NTMCs. Interestingly, studies for 2D NTMCs are becoming a hot topic in the 2D field with the joint effort of related scientists, which is unexpected. Previously, we launched a series of studies to develop new NTMCs and investigate their properties and applications, whose details are shown below. For PtS_2, we, together with coworkers, experimentally and theoretically demonstrated that 2D layered PtS_2 presents an extraordinarily strong interlayer interaction compared to other 2D materials, whose bandgap can be tuned from 0.25 eV in bulk to 1.6 eV for a monolayer owing to the strong hybridization between the *d* orbitals of Pt atoms and the p_z orbitals of S atoms.[1] Subsequently, we introduced 2D $PdSe_2$ with a unique puckered pentagonal structure to the 2D family, whose few layers were successfully engineered into an ambipolar FET with high electron mobility of 216 $cm^2V^{-1}s^{-1}$.[10] Very recently, we developed a new high-effect catalyst based on amorphization of $Pd_3P_2S_8$ nanodots, which exhibits excellent electrocatalytic activity towards the hydrogen evolution reaction with an onset potential of −52 mV, a Tafel slope of 29 mV dec^{-1} and outstanding long-term stability.[19] The discovery of these new 2D NTMCs opens up a new platform to develop high-air-stable 2D materials for practical applications in the fields of electronics, optoelectronics, and catalysis. However, only a few 2D NTMCs[1,5–8,10–12,14,17,19,22–24] are discovered, greatly limiting their applications, which may be solved by developing new 2D NTMCs.

To drive the continuing development of 2D NTMCs, herein, we introduce a new ternary van der Waals (vdW) NTMC: Ta_2PdS_6 to 2D family, which was successfully prepared in the form of ribbon-like crystals via solid-state reactions with the help of a mineralizer agent, iodine (I). Ta_2PdS_6 crystallizes a layered structure with the orthorhombic space group *C*2/*m* consisting of unique $^2_\infty[Ta_6PdS_6]$ layers with PdS_4 quadrilaterals and TaS_7 polyhedra as well as vdW gaps between the layers. It is found that Ta_2PdS_6 displays a semiconducting behavior with a strong layer-dependent bandgap that can be tuned from near 0 eV in bulk to 1.0 eV for a monolayer. Interestingly, a FET based on a trilayer Ta_2PdS_6 nanowire delivers impressive performance with electron mobility of ≈25 $cm^2V^{-1}s^{-1}$, I_{on}/I_{off} ratio of 10^6, and one year of air stability, which is better than most reported 2D materials-based devices. More interestingly, such a trilayer Ta_2PdS_6 device also exhibits excellent optoelectronic performance with a photoresponsivity of ≈1.42×10^6 A W^{-1}, detectivity of ≈7.1×10^{10} Jones, and a photoconductive gain of 2.7×10^6 under illumination by a 633 nm laser with a power of 0.025 W m^{-2}. Studies of the device band profiles reveal that the high optoelectronic performance can be ascribed to a photogating effect. In addition, our device also delivers a good broadband photoresponse ranging from 450 nm to 1450 nm. Our results demonstrate the potential for Ta_2PdS_6 thin crystals as a new 2D material in nano-optoelectronic devices.

Ta_2PdS_6 crystallizes with a monoclinic space group *C*2/*m* (No. 12),[25] which features a layered structure (Figure 1a), with unique $^2_\infty[Ta_6PdS_6]$ layers approximately oriented parallel to the plane $(\bar{2}01)$, which are composed of PdS_4 quadrilaterals and TaS_7 polyhedra (Figure 1b). According to the definition of monolayer thickness, $d_{1L} = d_{1L,\ atomic} + d_{gap\ between\ two\ adjacent\ layers}$, the theoretical thickness of the monolayer is approximately 0.7 nm, as shown in Figure 1a. Single crystals of bulk Ta_2PdS_6 were synthesized by solid-state reaction with iodine (I) as a flux agent (Figure 1c, see Experimental Section for details), whose pure phase is confirmed by measurement of the X-ray powder diffraction (XRD) pattern (Figure 1d). Unlike traditional 2D bulk materials exhibiting platelet-like shapes, for example, MoS_2, $SnSe_2$, etc., bulk Ta_2PdS_6 crystallizes into shiny, needle-like shapes (inset of Figure 1d, top of Figure 1e), because the value for the *b*-axis cell lattice parameter of 3.27 Å is much smaller than the *a*-axis and *c*-axis parameters of 9.97 and 11.69 Å, respectively, leading to the long axis of the single crystals being orientated along the *b*-axis. In addition, it is noted that the atomic ratios of the obtained single crystals are close to the stoichiometric ratio of 2:1:6, confirmed by the energy dispersive X-ray (EDX) result of $Ta_{1.8(3)}Pd_{1.1(2)}S_{6.2(5)}$ (Figure 1e) and X-ray photoelectron spectroscopy (XPS) result of $Ta_2Pd_{0.96}S_{6.06}$ (Figure S1, Supporting Information).

Ta_2PdS_6 atomic layers were obtained by micro-mechanically exfoliating bulk Ta_2PdS_6 onto SiO_2/Si (285 nm thick SiO_2) using adhesive tape for the first time. It is noted that the widths of the obtained Ta_2PdS_6 needle-like crystals are very narrow (a few microns to tens of microns) such that most of the bulk crystals are exfoliated into nanowires and only a few bulk crystals can be exfoliated into nanoflakes with a width of tens of microns (Figure 2a,b). The experimental thicknesses of the monolayer and bilayer are determined to be ≈0.9 and 1.9 nm, respectively, using atomic force microscopy (AFM) measurements (inset, Figure 2a), which is basically consistent with the theoretical values of 0.7 nm and 1.4 nm, respectively. In addition, the atomic structure of the few-layer Ta_2PdS_6 nanowires along the [203] axis (Figure 2b,c) is confirmed by atomically resolved annual dark-field (ADF) scanning transmission electron microscopy (STEM), which is found to match well with the simulated structure (inset, Figure 2c). To further confirm the atomic structure of Ta_2PdS_6, an atomic resolution ADF-STEM image of few-layer Ta_2PdS_6 along the [200] axis (Figure 2d,e) is recorded, in which the distances between the atoms are found to be well fitted to the simulated values (Figure 2f), suggesting that the atomic structure of the few layers is consistent with the structure of the bulk. The invariance of the atomic structure of the few layers is also supported by STEM EDS elemental mapping (Figure 2g,j), which shows good distribution uniformity for the three elements in the few-layer sample.

Bulk Ta_2PdS_6 has been proven to be a semiconductor, but slight variation in the conductivity with temperature leads to a small bandgap for bulk Ta_2PdS_6,[25] combined with theoretical results that the calculated bandgap is 0 eV, revealing that the real bandgap should be close to 0 eV. Especially, the bandgap can be tuned from close to 0 eV for the bulk to 1.0 eV for the monolayer (Figure S2, Supporting Information), in which the bandgap of the trilayer calculated to be approximately 0.79 eV, basically agreeing with the experimental value of 0.82 eV (Figure S3, Supporting Information). The small difference between the experimental and calculated bandgaps should be attributed to the inaccurate description of the eigenvalues for the electronic states in density functional theory (DFT) calculations.[26] Such strong layer-dependence stems from strong hybridization between the *d* orbitals of the Pd atoms and the *p* orbitals of the

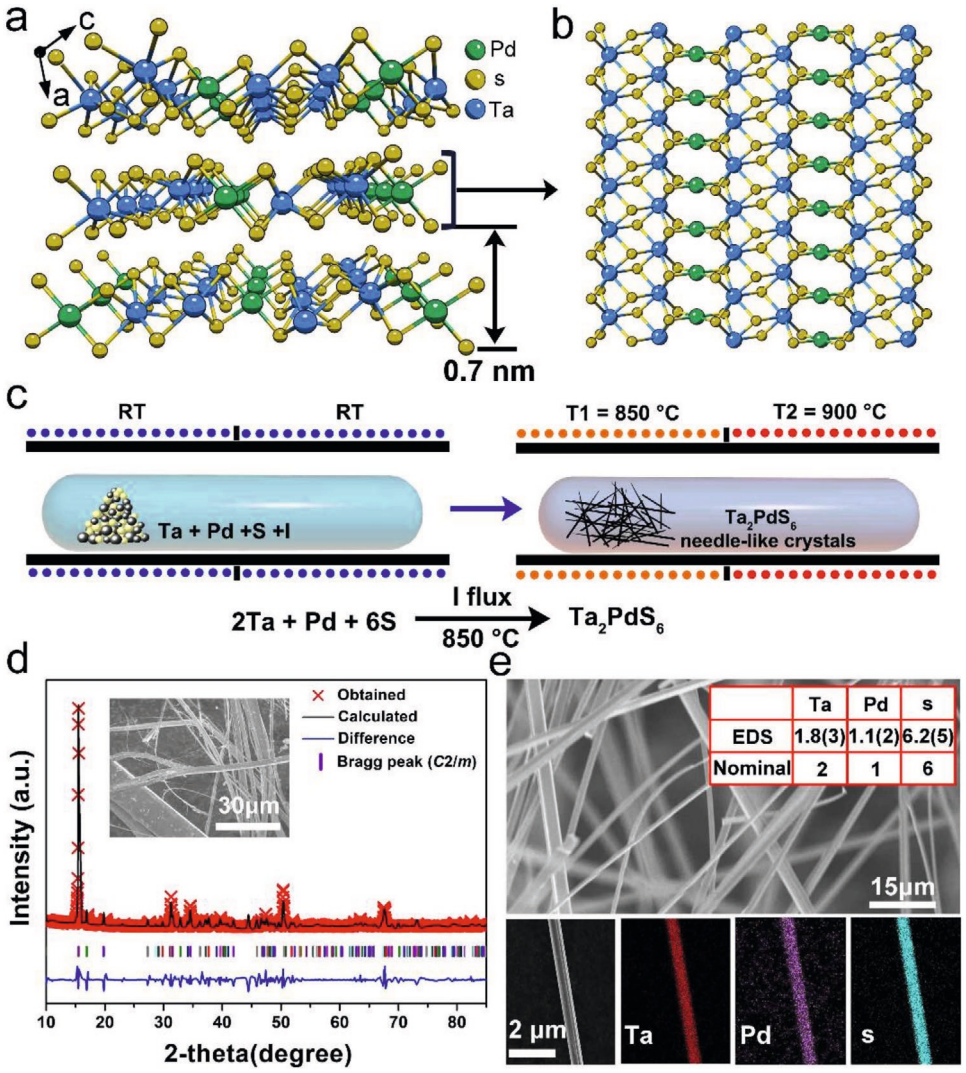

Figure 1. Synthesis and crystal structure of layered Ta_2PdS_6. a) Crystal structure of Ta_2PdS_6 viewed along the *b*-axis, showing that the expected thickness of the monolayer is ≈0.7 nm. b) Projection of the structure of monolayer Ta_2PdS_6 onto the $(\bar{2}01)$ plane. Green: Fe atoms, yellow: s atoms, blue: Pt atoms. c) Schematic diagram of the growth of Ta_2PdS_6 single crystals from the precursors of tantalum powder, palladium powder, sulfur powder, and iodine particles. d) Experimental and simulated X-ray powder diffraction (XRD) patterns for Ta_2PdS_6. e) Upper panel: SEM image and EDS result for the as-synthesized bulk Ta_2PdS_6. Lower panel: EDS elemental mapping for a typical Ta_2PdS_6 crystal.

S atoms, which was found in other NTMCs as well, for example, PtS_2,[1] $PdSe_2$,[8] $PtSe_2$,[5] etc. The lattice dynamics for the material originates from the interactions between elementary excitations and phonons, which is often used for probing the origin of its physical properties. However, to date, the vibrational properties of Ta_2PdS_6 have not been reported. Here, we systematically investigate the Raman vibrational properties by DFT calculations and Raman spectroscopy. Group theory analysis indicates that there are twelve Raman vibrational modes in the two categories of A_g (8) and B_g (4) since Ta_2PdS_6 belongs to the space group $C2/m$ (point group C_{2h}), that is, A_g^1, A_g^2, A_g^3, A_g^4, A_g^5, A_g^6, A_g^7, A_g^8, B_g^1, B_g^2, B_g^3, and B_g^4, for which the phonon vibrational details are shown in Figure S4, Supporting Information. Figure 3a shows that the experimental phonon frequencies for the bulk sample agree well with the calculated results, including the number and peak positions for the Raman modes. In addition, the dependence of the Raman spectra on the number of layers is studied, as shown in Figure 3b,c (low-frequency Raman spectra) and Figure 3d,e (high-frequency Raman spectra). In the low-frequency region (40–110 cm^{-1}), there are two Raman peaks: B_g^1 and A_g^1, in which B_g^1 show a small redshift as the thickness is increased from 1L to bulk accompanied with the disappearance of the peaks for the monolayer and bilayer, yet, the A_g^1 positions do not basically change with increasing thickness (Figure 3b,c). For the high-frequency region, there are ten Raman peaks that do not show the blueshifts or redshifts; however, some of these peaks disappear in the particular layers, for example, A_g^1 in 1L, B_g^3 and A_g^3 from 1L to 3L, B_g^4 in 1L, A_g^6, A_g^7, and A_g^8 in 1L, which is possibly due to the weak intensities of these vibrational modes in the particular layers.

To evaluate the electronic transport properties of few-layered Ta_2PdS_6, we fabricated a back-gated FET based on a

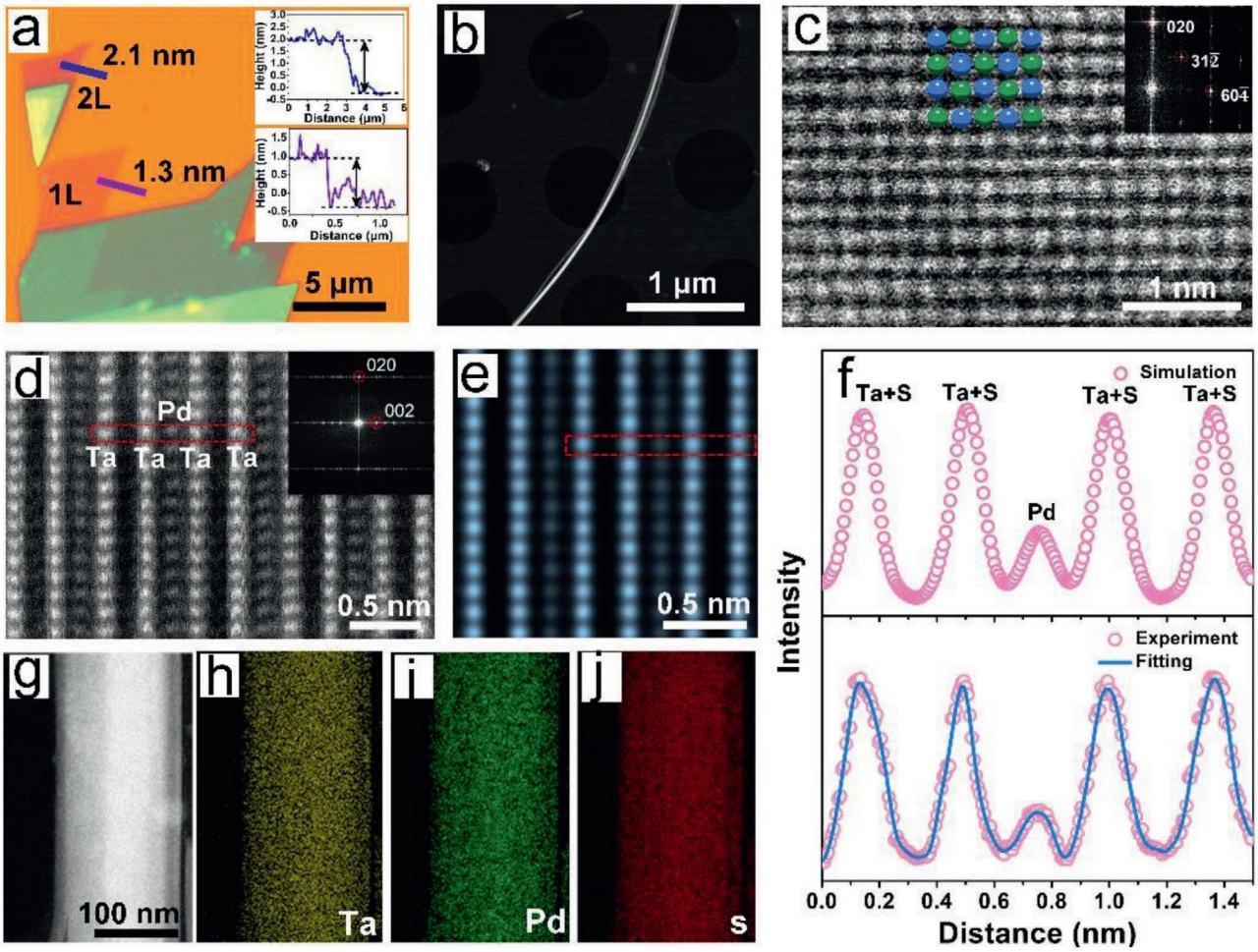

Figure 2. AFM and STEM characterization of few-layer Ta_2PdS_6 nanosheets. a) Optical image of Ta_2PdS_6 nanosheets on a Si/SiO_2 substrate; the insets show the AFM results for a monolayer and bilayer, which show that the thicknesses of the monolayer and bilayer are ≈1.3 and 2.1 nm. b) Low-magnification ADF-STEM image of a few-layer Ta_2PdS_6 nanowire. c) High-magnification ADF-STEM image of few-layer Ta_2PdS_6 viewed along the [203] axis; the left and right insets show the simulated structure and the corresponding fast Fourier-transform (FFT) pattern, respectively. d,e) Atomic resolution ADF-STEM image of few-layer Ta_2PdS_6 viewed along the [200] axis; the inset shows the corresponding FFT pattern. f) Line intensity profile of the rectangular region in (d) and (e). g–j) EDS elemental mapping for a typical Ta_2PdS_6 nanosheet. Blue: Ta, green: Pd, red: S.

few-layer Ta_2PdS_6 nanowire on a SiO_2/Si (280 nm oxide layer) substrate (Figure 4a). The AFM confirms the thickness of the Ta_2PdS_6 nanowire to be ≈2.4 nm, that is, three layers for the channel material used (Figure 4b). The transfer curves (I_{ds}-V_{bg}) on the linear (blue ball in Figure 4c) and logarithmic (red ball in Figure 4c) scale are obtained by sweeping the back-gate voltage from −60 V to 60 V, revealing that Ta_2PdS_6 is an *n*-type semiconductor due to the increase in current observed with increasing gate voltage, a threshold voltage of $V_{th} \approx -21$ V, as well as an I_{on}/I_{off} ratio that reaches 10^6. To the best of our best knowledge, this I_{on}/I_{off} ratio is the highest record for 2D NTMCs at room temperature (RT) and higher than that reported for most 2D materials with a similar device structure. In addition, the electron mobility can be estimated from the linear region in the transfer curve with the following equation:[27]

$$\mu = \frac{L}{W \times C_i} \times \frac{dI_{ds}}{dV_G} \times \frac{1}{V_{ds}} \tag{1}$$

where L, W, and C_i denote the channel length,[28] width, and the oxide capacitance per unite area, respectively. V_{ds}, I_{ds}, and V_G denote the source-drain bias, current, and bottom gate voltage, respectively, in the linear region in the I_{ds}–V_{bg} curve. Considering the non-negligible fringing effect derived from the narrow width of Ta_2PdS_6 nanowire channel, the finite element methods with COMSOL MULTIPHYSICS v4.3b is used to calculate the capacitance and C_i can be estimate the mobility from the following equation:[29]

$$C_i = \frac{C}{WL} = \frac{2\pi\varepsilon_r\varepsilon_0}{W\ln(2t/R)} \tag{2}$$

where C_i is the capacitance, ε_0 and ε_r are the vacuum dielectric constant and the dielectric constant of SiO_2 (ε_r = 3.9), t is the distance between the silicon substrate and the center of the nanowire, and R is the height of the nanowire. The electron mobility in our device was calculated to be ≈25 $cm^2V^{-1}s^{-1}$, which can be comparable to the intrinsic mobilities of most 2D

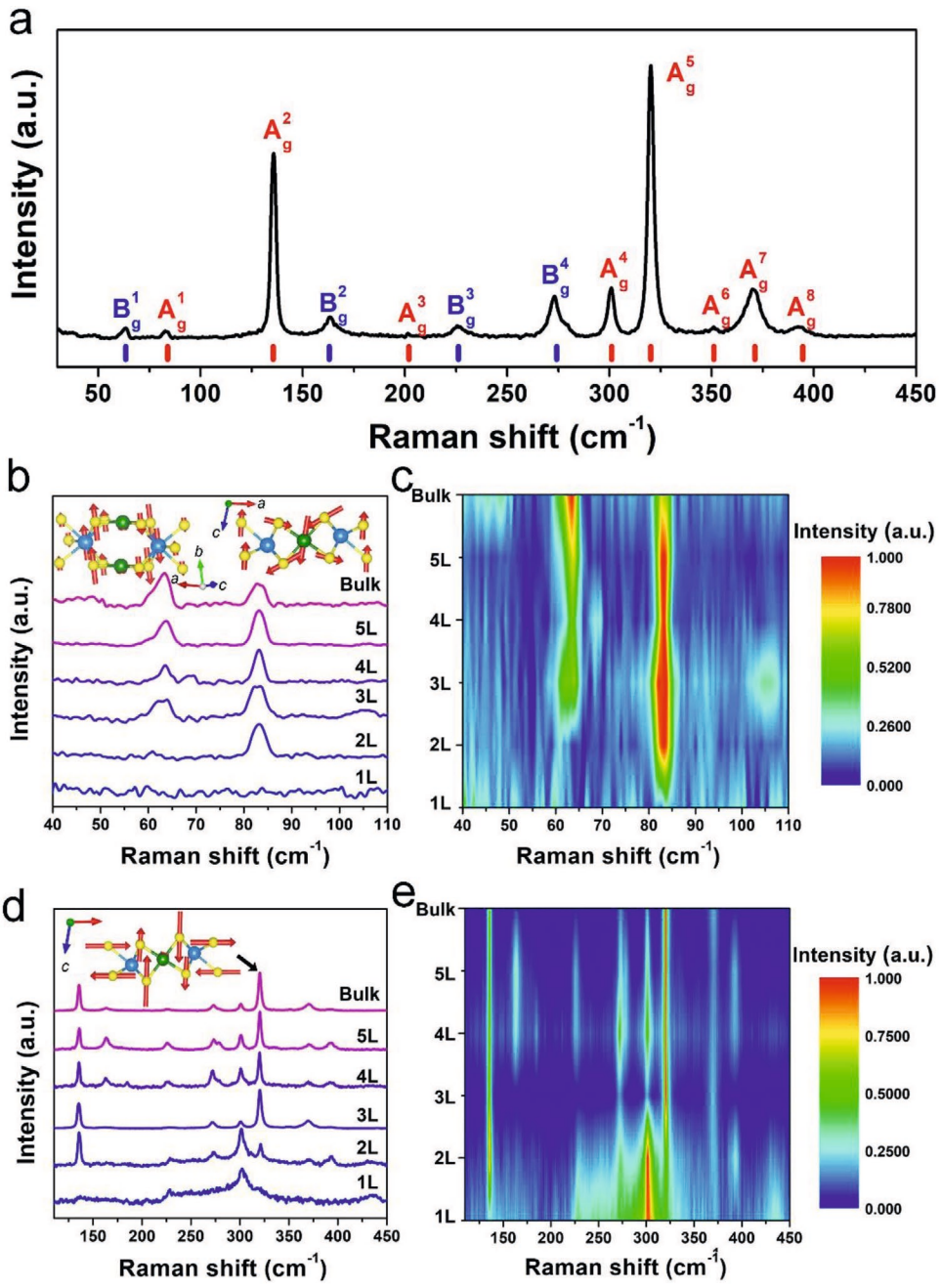

Figure 3. Raman characterization of layered Ta_2PdS_6. a) Experimental Raman spectrum (solid black line) for bulk Ta_2PdS_6 and the corresponding calculated frequencies (vertical bars, lower panel). b–e) Raman spectra ((b) and (d)) and intensities ((c) and (e)) obtained for Ta_2PdS_6 samples ranging from a monolayer to the bulk in the low-frequency (40–110 cm^{-1}) and high-frequency (110–450 cm^{-1}) regions; the insets in (b) show the calculated phonon vibrational patterns for the B_g^1 and A_g^1 modes; the inset in (d) shows the calculated phonon vibrational pattern for the A_g^5 mode.

materials determined from experimental results. Considering the existence of a large number of surface traps or impurities on the SiO_2/Si surface that can degrade the carrier mobility by scattering from charged impurities, the carrier mobility in Ta_2PdS_6 FETs can be further improved by reducing the number of surface traps/impurities or using high-κ gate dielectric materials, which is proved to increase the carrier mobility in MoS_2 from 0.1 cm^{2}V^{-1}s^{-1} to 200 cm^{2}V^{-1}s^{-1}.[30] In addition, the mobility can also be improved by optimizing the crystal quality, reducing the contact resistance, and tuning the channel layer thickness. Therefore, further improvement in the carrier mobility in Ta_2PdS_6 FETs can be achieved by optimizing the above conditions in future work. Noted that when the device was exposed in air for one year, the I_{on}/I_{off} ratio and electron mobility do not show degeneration (Figure 4e), which reveals that few-layered Ta_2PdS_6 exhibits ultrahigh air stability. Such high air stability may be attributed to the strong Pd-S bonding as a result of the strong hybridization between the *d* orbitals of

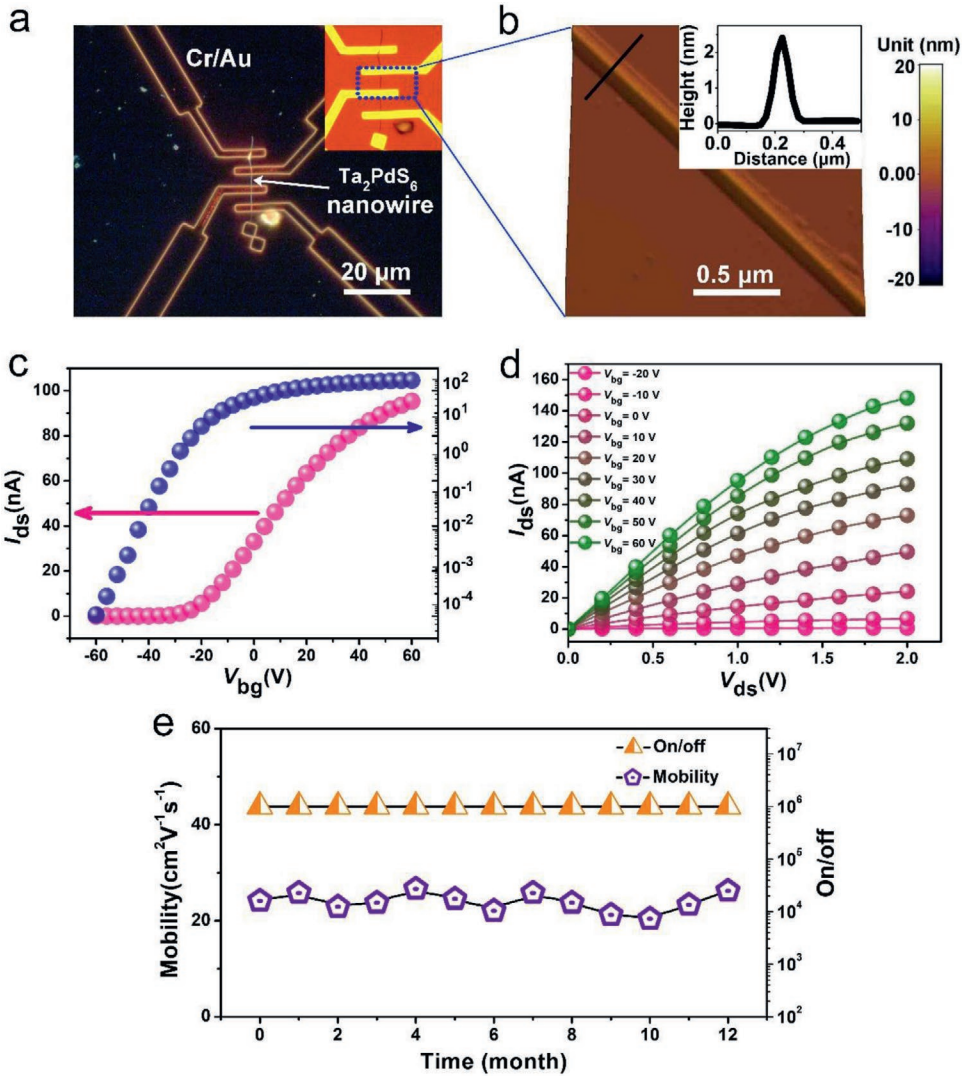

Figure 4. Basic electrical performance characteristics for the trilayer Ta_2PdS_6 nanowire-based transistor. a) The dark-field and bright-field (the inset) optical images of the trilayer Ta_2PdS_6 FET device with Cr/Au as electrodes on a Si/SiO_2 substrate. b) AFM image of the channel material for the FET, showing that the channel material is the trilayer Ta_2PdS_6 nanowire. c) The room temperature transfer characteristics, I_{ds}-V_g curves for an as-fabricated trilayer FET plotted on a linear (red) and log scale (blue) with a source-drain voltage (V_{ds}) of 1 V. d) The output characteristics, I_{ds}–V_{ds} curves for the same trilayer FET but at different bottom gate voltages in the range of –60 and 60 V. e) The stable characteristics, FET mobility (triangle) and On/Off ratio (pentagon) as a function of time, showing that the as-fabricated trilayer Ta_2PdS_6 FET possesses high stability.

palladium and the *p* orbitals of sulfur. The moderate mobility, high I_{on}/I_{off} ratio, as well as ultrahigh air stability, make Ta_2PdS_6 a competitive FET channel material compared with other 2D semiconductors.

The abovementioned trilayer Ta_2PdS_6 nanowire-based FET devices are used to demonstrate the optoelectronic properties of few-layered Ta_2PdS_6, which is excited by continuously focused lasers with varying power and continuous wavelengths from 450 nm to 1450 nm (Figure 4a). In this work, the 633, 1064, and 1450 nm laser-induced photoresponse was deeply studied to probe the basic optoelectronic properties of trilayer Ta_2PdS_6 and the photocurrent mechanism. First, the transfer curve for the phototransistor was measured under illumination by a 633 nm laser with different powers (Figures S5, S6, Supporting Information), in which the photocurrent I_{ph} is extracted by using the following expression: $I_{ph} = I_{ds,\ light} - I_{ds,\ dark}$, where $I_{ds,\ light}$ and $I_{ds,\ dark}$ is the source-drain current under illumination and in the dark condition, respectively. Figure 5b shows the gate-dependent photocurrent I_{ph}, transconductance g_m, and dark current curves in the top, middle, and bottom panels, respectively, suggesting that the photoresponse dependence of the electrostatic gating effect should be divided into three distinct regions, as marked in the bottom panel of Figure 5a. In region I, the photocurrent generated increases with the incident power and the gate bias in the off state, as found in most *n*-type 2D semiconductors, for instance, MoS_2,[30] PtS_2,[31] and GaTe.[32] Especially, the photocurrent is found to peak at $V_{bg} = -18$ V in region II when a light p-doped channel is induced near the on-state due to the decreasing photocurrent with increasing gate bias ($V_{bg} > -18$ V). However, when the V_{bg} increases into region

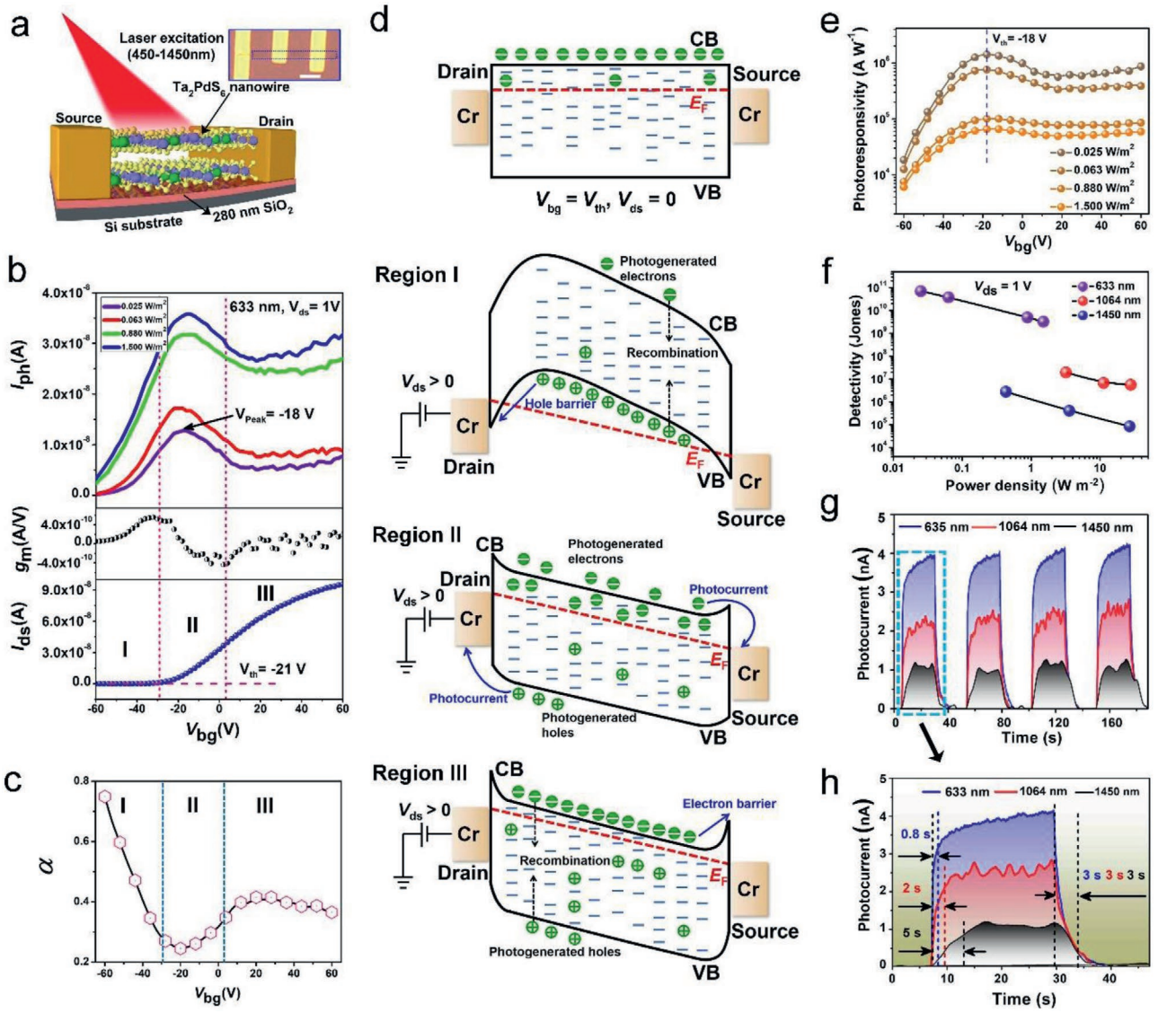

Figure 5. Optoelectronic properties of the trilayer Ta_2PdS_6 nanowire-based phototransistor. a) Schematic diagram of the phototransistor composed of a trilayer Ta_2PdS_6 nanowire (dotted box in upper panel) on a SiO_2/Si wafer with laser illumination. b) Top panel: the gate-dependent photocurrent (top) the phototransistor under varying excitation power. Middle panel: the gate-dependent transconductance of the phototransistor. Bottom panel: phototransistor transfer characteristic. $V_{ds} = 1$ V, $\lambda_{excitation} = 633$ nm. c) Exponent (α) extracted from panel (b) for each V_{bg}. d) Schematics for the device band profiles in the bottom panel of (b) for different regions of the transfer curve, accounting for the distinct photoresponse characteristics in the three regions. Region I: hole concentration increases as gate voltage becomes more negative to produce a big hole barrier so that a reduced photocurrent is observed. Region II: photogating effect is dominant as a result of the partially occupied hole trap states prolonging the photogenerated electron lifetime. Region III: the photogenerated electrons suffer from severe scattering and electron-hole recombination due to a high free electron concentration and high higher electron barrier. E_F Fermi level; CB, conduction band; VB, valence band. Black dots, electrons; open circles, holes. e) Dependence of the photoresponsivity on the gate bias under 633 nm laser illumination with varying laser power at $V_{ds} = 1$ V. f) Photoresponsivity as a function of excitation power excited by a laser wavelength of 633, 1064, and 1450 nm, respectively. $V_{ds} = 1$ V, $V_{bg} = -18$ V. g,h) Time-resolved photoresponse of the device at a bias voltage of 0.5 V and a gate voltage of −50 V under laser illumination at a wavelength of 633, 1064, and 1450 nm, respectively.

III, the gate-dependent photocurrent curve flattens because the photocurrent only changes slightly with increasing gate bias.

Generally, there are two types of photocurrent generation mechanisms for the 2D material-based photodetector. One originates from the excitation of free carriers as a result of optical transitions, including the photovoltaic effect, photoconductive effect, and photogating effect. Another is attributed to a thermal effect, including the photothermoelectric and bolometric effects. As a new layered material, there is no report to date for the photocurrent generation mechanism of Ta_2PdS_6. Based on the operational conditions used in this work, the photocurrent generated from the thermal effect should be neglected and the photovoltaic effect should not be considered due to the closed-circuit rather than open-circuit conditions. For most 2D semiconductors-based phototransistors, the photogenerated current can be attributed to the conventional photoconductive effect,

in which excess photoinduced carriers are separated by an applied bias V_{ds} to give rise to an elevated current, leading to a reduced resistance for the semiconductor. The photoconductive effect is most obvious at low carrier concentration because carriers with low concentration suffer less scattering and recombination; thus, photocarriers can be efficiently collected by the electrode. In addition, an important signature of the photoconductive effect is the linear relationship between the photocurrent and light power density ($I_{ph} \propto P$). The photogating effect is a particular case of the photoconductive effect, in which photogenerated holes or electrons are trapped in trap states to produce a localized floating gate, effectively modulating the transistor threshold voltage V_{th}. The induced photocurrent can be expressed as follows: $I_{ph} = g_m \cdot \Delta V_{th}$, where $g_m = \frac{dI_d}{dV_g}$ is the transconductance of the transistor and ΔV_{th} is the shift in the threshold voltage. In general, the trapped type of photocarriers will prolong the recombination lifetime ($\tau_{lifetime}$) of the other type of photocarriers, resulting in a large photoconductive gain (G) according to $G = \tau_{lifetime}/\tau_{transit}$, where $\tau_{transit}$ is the transit time. One signature of the photogating effect is that the photoconductive gain decreases as the incident light power increases, that is, the photocurrent increases sublinearly with the incident light power density because the number of localized trap states is limited. For the Ta_2PdS_6 nanowire-based phototransistor, the threshold voltage V_{th} was observed to shift from −21 V to −18 V to −13 V for the dark condition and a 633 nm laser illumination with an incident light power density of 0.025 and 1.5 W m^{-2}, respectively (Figure 5b), which clearly manifests the existence of a photogating mechanism in this device. Based on the above discussion, it is noted that the photoconductive and photogating effects show a different power density-dependent photocurrent relationship ($I_{ph} \propto P^{\alpha}$), with $\alpha = 1$ for the former and $\alpha < 1$ for the latter, which also confirms the existence of a photogating effect in our device because α is less than 1 (Figure 5c).

The energy band diagram for the Ta_2PdS_6 channel and metal contacts is shown in Figure 5d, which can be used to explain the mechanisms operating in our device. In region I, the transistor is in the off-state and positively charged holes are induced into the channel to make the valence band bend downward at the Ta_2PdS_6/drain interface (Figure 5d), leading to a barrier for holes moving from the channel to the drain contact. Ta_2PdS_6 is an *n*-type semiconductor, so the concentration of hole carriers is low; thus, the photogating effect is negligible and the photoconductive effect dominates in region I, which is also confirmed by the low transconductance and the value of α being close to 1 (Figure 5b,c). When a larger negative gate bias is applied, the photogenerated holes suffer from severe scattering and recombination, resulting in a smaller photocurrent (Figure 5b). In region II, following application of a higher gate voltage, E_F moves to higher energy and the band becomes almost flat, leading to switching of the transistor to the on-state and a decrease in the concentration of free holes with increasing free electron concentration, accompanied by the coexistence of hole and electron trap states. When the gate bias reaches ≈−18 V, the electron trap states are mostly occupied by free electrons, but the hole trap states are partly occupied by photogenerated holes, which prolongs the photogenerated electron lifetime. Meanwhile, the electron transport barrier is at the minimized level to produce the shortest electron transit time, giving rise to a large photoconductive gain G ($G = \tau_{lifetime}/\tau_{transit}$) and maximized photocurrent (Figure 5a, top panel). As a result, the photogating effect is dominant in region II, which is also identified by the fact that the value of α is far lower than 1 (Figure 5c). In region III, a positive gate bias is applied and the corresponding channel is n-doped with the valence band bends downward at the Ta_2PdS_6/source interface, leading to a barrier for electrons moving from the channel to the source. In this region, the concentration of free electrons in the conduction band is high but the concentration of free holes in the valence band is low, leading to the electron trap states becoming fully occupied by electrons but with the hole trap states nearly empty in the dark condition. After illumination, electron-hole pairs are generated and the photogenerated holes are subsequently trapped in the hole trap states (Figure 5d), which prolongs lifetime of the photogenerated hole, leading to a large photoconductive gain. Therefore, the photogating effect is dominant in region III, which is also confirmed by a value of α far smaller than 1 (Figure 5c), as found for region II. However, when a larger positive gate bias is applied, the heavily n-doped channel produces a higher electron barrier to make the electrons suffer from severe scattering and electron-hole recombination, resulting in a repressed photocurrent (Figure 5b, top panel).

Photoresponsivity (R) is a key figure of merit parameter for evaluating the performance of the phototransistor, which is defined by $R = I_{ph}/P$, where I_{ph} is the photocurrent flowing in the device and P is the incident optical power. Based on the photogating effect in our device, under 633 nm-laser illumination, the photoresponsivity can be continuously tuned by the gate bias (Figure 5e), in which a peak responsivity of ≈1.42×10^6 A W^{-1} is achieved at a gate bias of ≈−18 V and light power of 0.025 W m^{-2}, which is one of the highest recorded values among all 2D material-based phototransistors.[6,11,31–39] It is also noted that an increased responsivity was observed with reduced excitation power (Figure 5e,f), which is possibly attributed to the less frequent carrier recombination and longer carrier lifetime at weaker illumination. In addition, the dependence of photoresponsivity on the light power at a wavelength of 1064 and 1450 nm is also shown in Figure 5g, Figures S7 and S8, Supporting Information, manifesting that the highest responsivities are ≈420 and 60 A W^{-1}, respectively, which are lower than that obtained at 633 nm due to the smaller optical absorptions resulting from the lower photon energies. Furthermore, the cyclability of the phototransistor under illumination by a laser at a wavelength of 633, 1064, and 1450 nm is checked with a bias voltage of 0.5 V and a gate voltage of −50 V (Figure 5g), which shows little deviation in the duration cycles, suggesting that the photoresponse of our device is reversible and stable. The rise time/decay time is also an important figure of merit, which is defined as the time over which the stable photocurrent varies from 10/90% and 90/10% when the laser is switched on or off, respectively. Figure 5h shows that our device displays a moderate response rate with a rise time and decay time of ≈0.8 s and 3 s, ≈2 s and 3 s, and ≈5 s and 3 s for 633, 1064, and 1450 nm laser illumination (Figure 5h), respectively. The seconds-level response time of our devices is not fast compared to most of 2D materials-photodetectors,[40–42], for example, 6 ms/20 ms of Bi_2Se_2O,[43]

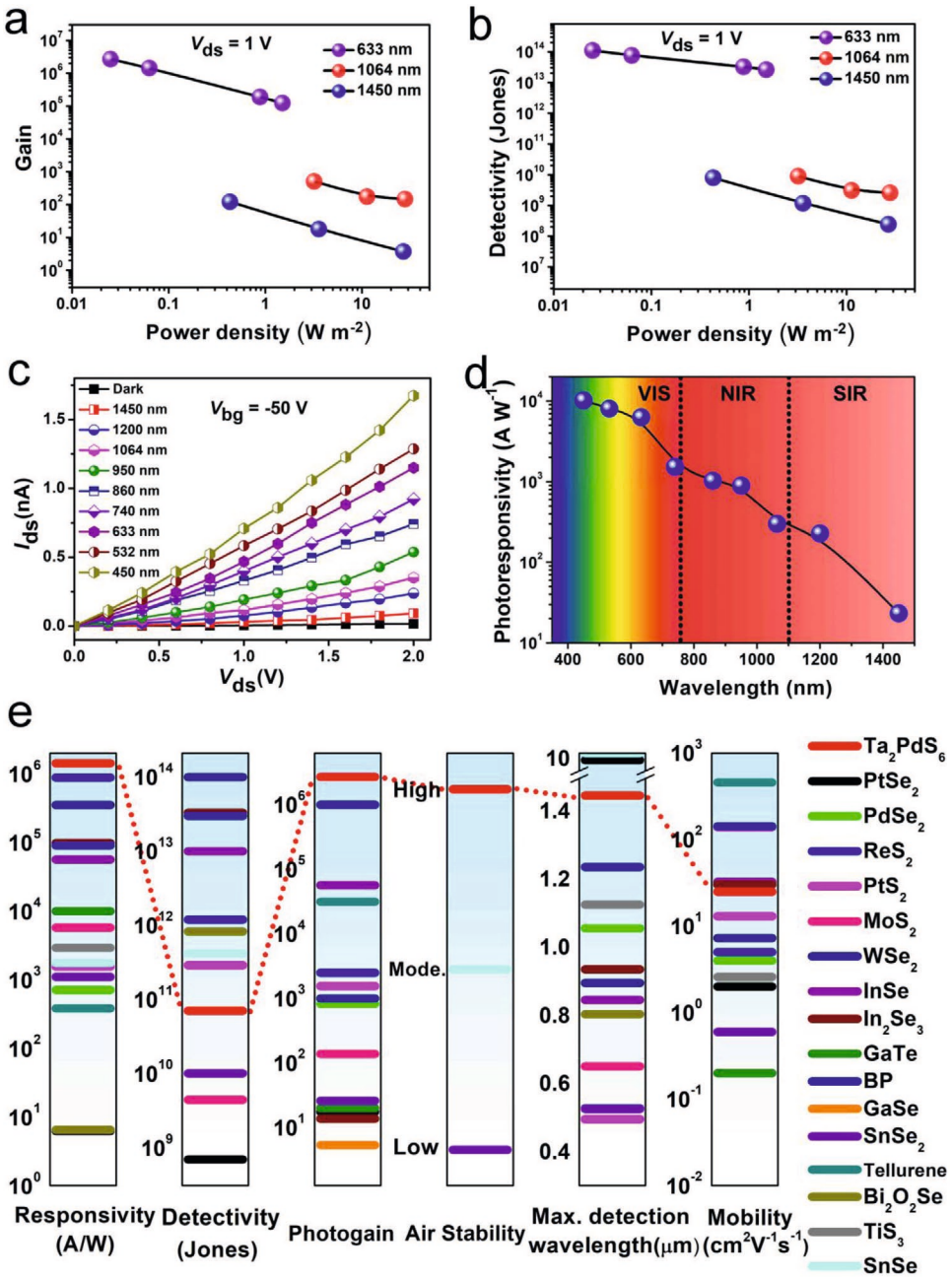

Figure 6. The power-dependence of the a) photoconductive gain and b) detectivity for a trilayer Ta_2PdS_6 nanowire-based phototransistor excited by a laser with a wavelength of 633, 1064, and 1450 nm, respectively. V_{ds} = 1 V. c) I_{ds}-V_{ds} curves for the phototransistor under laser illumination at different wavelengths ranging from 450 nm to 1450 nm with a laser power intensity of approximately 3.3 W m^{-2}. V_{bg} = −50 V. d) The excited wavelength-dependence of the photoresponsivity of the phototransistor under a laser excitation power of ≈3.3 W m^{-2}. V_{bg} = −50 V, V_{ds} = 1 V. e) Comparison of high-performance phototransistors based on 2D materials, including $PtSe_2$,[11] $PdSe_2$,[6] ReS_2,[29] PtS_2,[27] MoS_2,[31] WSe_2,[34] InSe,[33] In_2Se_3,[32] GaTe,[28] black phosphorus (BP),[30] GaSe,[35] $SnSe_2$,[36] Tellurene,[48] Bi_2O_2Se,[49] TiS_3,[27] and SnSe.[50]

400 μs/200 ms of MoS_2,[44] which should be attributed to the photogating effect.

Photoconductive gain (G) is used to evaluate the ability of detected charge carriers per single incident photon, which is defined as $G = \tau_{lifetime}/\tau_{transit}$ (abovementioned) = $Rh\nu/q\eta$, where $h\nu$ is the photon energy, η is the absorption of the channel, and q is the unit of charge. Figure 6a shows that the photoconductive gain decreases as the laser power increases at an incident laser wavelength of 633, 1064, and 1450 nm, which is due to improved frequent carrier recombination and reduced carrier lifetime with increasing light power. It is noted that a maximal photoconductive gain of approximately 2.7 × 10^6 is achieved by using a 633 nm laser and a bias voltage of 1.0 V, which is superior to that obtained by the vast majority of reported 2D material-based photodetectors. Meanwhile, maximum external photoconductive gains of 508 and 121 are

achieved for NIR light with a wavelength of 1064 nm and shortwave infrared (SIR) light with a wavelength of 1450 nm. The high photoconductive gain of our device can be attributed to a long lifetime for holes, resulting from the trapping of holes and the short electron transit time due to the high electron mobility. Moreover, the detectivity is one of the most important figures of merit, representing the sensitivity to distinguish the background noise, which is given by $D^* = (S\Delta f)^{1/2}/\mathrm{NEP}$, where S is the effective area of the device, Δf is the electrical bandwidth in Hz, and NEP is the noise equivalent power. The actual noise, including the shot noise, thermal Jounson noise and $1/f$ noise[45,46] is checked (Figure S9, noise measurement in Supporting Information), which displays that the noise of our device is dominated by $1/f$ noise at low frequency, similar to some 2D materials based photodetectors.[6,11] Figure 6b plots the detectivity under 633, 1064, and 1450 nm incident laser irradiation as a function of light intensity, revealing that, under illumination by a 633 nm laser, the maximal D^* can reach 7.1×10^{10} Jones ($V_{bg} = -18$ V, $V_{ds} = 1.0$ V). In addition, under illumination at 1064 and 1450 nm, maximum detectivities of 1.9×10^7 and 2.8×10^6 Jones were achieved at light intensities of 3.19 and 0.43 W m^{-2}, respectively.

The broadband photoresponse performance of the Ta_2PdS_6 nanowire-based transistor is investigated under the illumination of a 3.3 W m^{-2} fixed-intensity laser with different wavelengths ranging from 450 nm to 1450 nm (Figure 6c,d). Figure 6c shows the output curves (I_{ds}-V_{ds}) obtained under laser illumination at different wavelengths, revealing that our device shows a good broad spectral response to light in the ultraviolet to SIR regions. Moreover, it is worth noting that the photocurrent decreases as the light wavelength increases (Figure 6c); correspondingly, the photoresponsivity shows the same trend, which can be ascribed to the weaker optical absorption of the long wavelength light. The performance of the main 2D material-based photodetectors with their highest records is summarized in Figure 6e, including Ta_2PdS_6, $PtSe_2$,[11] $PdSe_2$,[6] ReS_2,[33] PtS_2,[31] MoS_2,[35] WSe_2,[38] InSe,[37] In_2Se_3,[36] GaTe,[32] black phosphorous (BP),[34] GaSe,[39] $SnSe_2$,[47] tellurene,[48] Bi_2O_2Se,[49] TiS_3,[27] and SnSe.[50] A comparison of the photoresponsivity, detectivity, photoconductive gain, air stability, maximum detection wavelength, and carrier mobility found for the abovementioned 2D devices and our fabricated Ta_2PdS_6 nanowire-based device shows that our device exhibits the excellent comprehensive performance. The excellent comprehensive optoelectronic performance makes 2D Ta_2PdS_6 a promising commercial optoelectronic channel material for various applications in image sensing, communications, environmental monitoring, remote control, etc.

In summary, we developed a new 2D material: Ta_2PdS_6 atomic layers, which can be obtained via high-temperature solid-state synthesis of bulk crystals and subsequent exfoliation of bulk crystals into thin crystals. An experimental and theoretical investigation reveals that the Ta_2PdS_6 atomic layers are semiconducting and their bandgaps can be tuned from near 0 eV for the bulk to 1.0 eV for a monolayer. A phototransistor based on a trilayer Ta_2PdS_6 nanowire was successfully fabricated, which is found to exhibit excellent electronic and optoelectronic performance, better than that shown by other 2D materials. This is attributed to the strong hybridization between the Pd and S atoms for the former and the photogating effect for the latter. Such high performance makes the multilayer Ta_2PdS_6 nanosheet or nanowire a promising candidate material for future sensitive optoelectronic applications.

Experimental Section

Synthesis and Mechanical Exfoliation of Ta_2PdS_6 Single Crystals: Single crystals of Ta_2PdS_6 were prepared by solid-state reaction with iodide as the fluxing agent. Stoichiometric amounts of high purity Ta, Pd, and S with a weight of 0.3 g and 120 mg of iodide were sealed in an evacuated 20 cm-long quartz tube under vacuum at 10^{-6} Torr, which was placed in a two-zone furnace (front section, Figure 1b). Next, the reaction zone was slowly heated up to 850 °C and held for 200 h with another zone held at 900 °C, preventing transport of the samples (back section, Figure 1b). After that, the furnace was naturally cooled down to RT and the products were collected in the reaction zone. Subsequently, the products were cleaned by using acetone to remove iodide, and, then, pure Ta_2PdS_6 single crystals with shiny, needle-like shapes were obtained (inset of Figure 1d, top of Figure 1e). Few-layer Ta_2PdS_6 was mechanically exfoliated from bulk crystals and transferred to a silicon substrate with a 280 nm thick silica layer using a scotch tape-based mechanical exfoliation method, which has been previously widely employed for the preparation of few-layer graphene and transitional metal dichalcogenides (TMDs).

TEM Sample Preparation and Image Simulations: The TEM sample was prepared by transferring the Ta_2PdS_6 exfoliated flakes onto an Au grid with a carbon film via a conventional wet-transfer method with the assistance of PMMA. Z-contrast STEM imaging was carried out with a modified JEOL 2100F equipped with a delta probe corrector, which is used to correct for aberration up to the 5th order, resulting in a probe size of 1.4 A. The imaging was conducted at an acceleration voltage of 60 kV. The convergent angle for illumination was ≈35 mrad, with a collection detector angle ranging from 62 mrad to 200 mrad.

Fabrication and Measurement of the Devices: The devices were fabricated by standard electron-beam lithography (EBL), and Cr/Au (10 nm/50 nm) contact electrodes were deposited using electron-beam evaporation. The channel length and width are 5 and ≈0.11 μm. The electronic and optoelectronic measurements were performed by using an Agilent B1500A Semiconductor Device Parameter Analyzer in a vacuum chamber of 10^{-3} Pa. Lasers with varying power and continuous wavelengths ranging from 450 nm to 1450 nm were used to investigate the photoresponse of the Ta_2PdS_6-based device. The laser spot with round shape has a typical diameter of ≈10 mm. The output powers of 633 nm laser used are 1.96 μW, 4.95 μW, 6.91 μW, and 0.12 mW, respectively. The output powers of 1064 nm laser used are 0.25, 0.88, and 2.2 mW, respectively. The output powers of 1450 nm laser used are 34 μW, 0.28 mW and 2.1 mW, respectively. The noise spectral density was acquired by a spectrum analyzer (SR 770) with source-drain bias supplied by Agilent B1500A at ambient conditions.

Supporting Information

Supporting Information is available from the Wiley Online Library or from the author.

Acknowledgements

This work was financially supported by "100 Top Talents Program" of Sun Yat-sen University (No. 29000-18841216) and "Young Teacher Foundation" of Sun Yat-sen University (No. 29000–31610036). This work was also supported by Youth Program of National Natural Science Foundation of China (No. 22006023) and Natural Science Foundation of Guangdong Province, China (No. 2019A1515010428).

Conflict of Interest

The authors declare no conflict of interest.

Keywords

noble-transition-metal chalcogenides, phototransistors, 2D materials

Received: August 18, 2020
Revised: November 13, 2020
Published online:

[1] Y. D. Zhao, J. S. Qiao, P. Yu, Z. X. Hu, Z. Y. Lin, S. P. Lau, Z. Liu, W. Ji, Y. Chai, *Adv. Mater.* **2016**, *28*, 2399.
[2] C. Yim, K. Lee, N. McEvoy, M. O'Brien, S. Riazimehr, N. C. Berner, C. P. Cullen, J. Kotakoski, J. C. Meyer, M. C. Lemme, G. S. Duesberg, *ACS Nano* **2016**, *10*, 9550.
[3] Z. G. Wang, Q. Li, F. Besenbacher, M. D. Dong, *Adv. Mater.* **2016**, *28*, 10224.
[4] X. Y. Chia, A. Adriano, P. Lazar, Z. Sofer, J. Luxa, M. Pumera, *Adv. Funct. Mater.* **2016**, *26*, 4306.
[5] Y. D. Zhao, J. S. Qiao, Z. H. Yu, P. Yu, K. Xu, S. P. Lau, W. Zhou, Z. Liu, X. R. Wang, W. Ji, Y. Chai, *Adv. Mater.* **2017**, *29*, 1604230.
[6] Q. Liang, Q. Wang, Q. Zhang, J. Wei, S. X. Lim, R. Zhu, J. Hu, W. Wei, C. Lee, C. Sow, W. Zhang, A. T. S. Wee, *Adv. Mater.* **2019**, *31*, 1807609.
[7] L. B. Luo, D. Wang, C. Xie, J. G. Hu, X. Y. Zhao, F. X. Liang, *Adv. Funct. Mater.* **2019**, *29*, 1900849.
[8] M. S. Long, Y. Wang, P. Wang, X. H. Zhou, H. Xia, C. Luo, S. Y. Huang, G. W. Zhang, H. G. Yan, Z. Y. Fan, X. Wu, X. S. Chen, W. Lu, W. D. Hu, *ACS Nano* **2019**, *13*, 2511.
[9] T. Y. Su, H. Medina, Y. Z. Chen, S. W. Wang, S. S. Lee, Y. C. Shih, C. W. Chen, H. C. Kuo, F. C. Chuang, Y. L. Chueh, *Small* **2018**, *14*, 1800032.
[10] W. L. Chow, P. Yu, F. C. Liu, J. H. Hong, X. L. Wang, Q. S. Zeng, C. H. Hsu, C. Zhu, J. D. Zhou, X. W. Wang, J. Xia, J. X. Yan, Y. Chen, D. Wu, T. Yu, Z. X. Shen, H. Lin, C. H. Jin, B. K. Tay, Z. Liu, *Adv. Mater.* **2017**, *29*, 1602969.
[11] X. C. Yu, P. Yu, D. Wu, B. Singh, Q. S. Zeng, H. Lin, W. Zhou, J. H. Lin, K. Suenaga, Z. Liu, Q. J. Wang, *Nat. Commun.* **2018**, *9*, 1545.
[12] A. D. Oyedele, S. Z. Yang, L. B. Liang, A. A. Puretzky, K. Wang, J. J. Zheng, P. Yu, P. R. Pudasaini, A. W. Ghosh, Z. Liu, C. M. Rouleau, B. G. Sumpter, M. F. Chisholm, W. Zhou, P. D. Rack, D. B. Geohegan, K. Xiao, *J. Am. Chem. Soc.* **2017**, *139*, 14090.
[13] H. F. Ma, P. Chen, B. Li, J. Li, R. Q. Ai, Z. W. Zhang, G. Z. Sun, K. K. Yao, Z. Y. Lin, B. Zhao, R. X. Wu, X. W. Tang, X. D. Duan, X. F. Duan, *Nano Lett.* **2018**, *18*, 3523.
[14] M. Z. Yan, H. Q. Huang, K. N. Zhang, E. Y. Wang, W. Yao, K. Deng, G. L. Wan, H. Y. Zhang, M. Arita, H. T. Yang, Z. Sun, H. Yao, Y. Wu, S. S. Fan, W. H. Duan, S. Y. Zhou, *Nat. Commun.* **2017**, *8*, 257.
[15] H. J. Noh, J. Jeong, E. J. Cho, K. Kim, B. I. Min, B. G. Park, *Phys. Rev. Lett.* **2017**, *119*, 016401.
[16] Y. L. Wang, L. F. Li, W. Yao, S. R. Song, J. T. Sun, J. B. Pan, X. Ren, C. Li, E. Okunishi, Y. Q. Wang, E. Y. Wang, Y. Shao, Y. Y. Zhang, H. T. Yang, E. F. Schwier, H. Iwasawa, K. Shimada, M. Taniguchi, Z. H. Cheng, S. Y. Zhou, S. X. Du, S. J. Pennycook, S. T. Pantelides, H. J. Gao, *Nano Lett.* **2015**, *15*, 4013.
[17] M. Sajjad, E. Montes, N. Singh, U. Schwingenschlogl, *Adv. Mater. Interfaces* **2017**, *4*, 1600911.
[18] S. H. Lin, Y. Liu, Z. X. Hu, W. Lu, C. H. Mak, L. H. Zeng, J. Zhao, Y. Y. Li, F. Yan, Y. H. Tsang, X. M. Zhang, S. P. Lau, *Nano Energy* **2017**, *42*, 26.
[19] X. Zhang, Z. M. Luo, P. Yu, Y. Q. Cai, Y. H. Du, D. X. Wu, S. Gao, C. L. Tan, Z. Li, M. Q. Ren, T. Osipowicz, S. M. Chen, Z. Jiang, J. Li, Y. Huang, J. Yang, Y. Chen, C. Y. Ang, Y. L. Zhao, P. Wang, L. Song, X. J. Wu, Z. Liu, A. Borgna, H. Zhang, *Nat. Catal.* **2018**, *1*, 460.
[20] M. Xu, T. Liang, M. Shi, H. Chen, *Chem. Rev.* **2013**, *113*, 3766.
[21] X. Y. Lin, W. Yang, K. L. Wang, W. S. Zhao, *Nat. Electron.* **2019**, *2*, 274.
[22] J. H. Lin, S. Zuluaga, P. Yu, Z. Liu, T. Pantelides, K. Suenaga, *Phys. Rev. Lett.* **2017**, *119*, 016101.
[23] D. K. Hu, T. Q. Zhao, X. F. Ping, H. S. Zheng, L. Xing, X. Z. Liu, J. Y. Zheng, L. F. Sun, L. Gu, C. G. Tao, D. Wang, L. Y. Jiao, *Angew. Chem., Int. Ed.* **2019**, *58*, 6977.
[24] A. Avsar, A. Ciarrocchi, M. Pizzochero, D. Unuchek, O. V. Yazyev, A. Kis, *Nat. Nanotechnol.* **2019**, *14*, 674.
[25] D. A. Keszler, P. J. Squattrito, N. E. Brese, J. A. Ibers, M. Shang, J. Lu, *Inorg. Chem.* **1985**, *24*, 3063.
[26] P. Miro, M. Ghorbani-Asl, T. Heine, *Angew. Chem., Int. Ed.* **2014**, *53*, 3015.
[27] J. O. Island, M. Buscema, M. Barawi, J. M. Clamagirand, J. R. Ares, C. Sanchez, I. J. Ferrer, G. A. Steele, H. S. J. van der Zant, A. Castellanos-Gomez, *Adv. Opt. Mater.* **2014**, *2*, 641.
[28] G. Horowitz, R. Hajlaoui, D. Fichou, A. E.l Kassmi, *J. Appl. Phys.* **1999**, *85*, 3202.
[29] O. Wunnicke, *Appl. Phys. Lett.* **2006**, *89*, 083102.
[30] B. Radisavljevic, A. Radenovic, J. Brivio, V. Giacometti, A. Kis, *Nat. Nanotechnol.* **2011**, *6*, 147.
[31] L. Li, W. K. Wang, Y. Chai, H. Q. Li, M. L. Tian, T. Y. Zhai, *Adv. Funct. Mater.* **2017**, *27*, 1701011.
[32] F. C. Liu, H. Shimotani, H. Shang, T. Kanagasekaran, V. Zolyomi, N. Drummond, V. I. Fal'ko, K. Tanigaki, *ACS Nano* **2014**, *8*, 752.
[33] E. F. Liu, M. S. Long, J. W. Zeng, W. Luo, Y. J. Wang, Y. M. Pan, W. Zhou, B. G. Wang, W. D. Hu, Z. H. Ni, Y. M. You, X. A. Zhang, S. Q. Qin, Y. Shi, K. Watanabe, T. Taniguchi, H. T. Yuan, H. Y. Hwang, Y. Cui, F. Miao, D. Y. Xing, *Adv. Funct. Mater.* **2016**, *26*, 1938.
[34] J. Wu, G. K. W. Koon, D. Xiang, C. Han, C. T. Toh, E. S. Kulkarni, I. Verzhbitskiy, A. Carvalho, A. S. Rodin, S. P. Koenig, G. Eda, W. Chen, A. H. C. Neto, B. Ozyilmaz, *ACS Nano* **2015**, *9*, 8070.
[35] D. H. Kang, M. S. Kim, J. Shim, J. Jeon, H. Y. Park, W. S. Jung, H. Y. Yu, C. H. Pang, S. Lee, J. H. Park, *Adv. Funct. Mater.* **2015**, *25*, 4219.
[36] J. O. Island, S. I. Blanter, M. Buscema, H. S. J. van der Zant, A. Castellanos-Gomez, *Nano Lett.* **2015**, *15*, 7853.
[37] W. Feng, J. B. Wu, X. L. Li, W. Zheng, X. Zhou, K. Xiao, W. W. Cao, B. Yang, J. C. Idrobo, L. Basile, W. Q. Tian, P. H. Tan, P. A. Hu, *J. Mater. Chem. C* **2015**, *3*, 7022.
[38] W. Zhang, M. H. Chiu, C. H. Chen, W. Chen, L. J. Li, A. T. S. Wee, *ACS Nano* **2014**, *8*, 8653.
[39] B. Mukherjee, Y. Q. Cai, H. R. Tan, Y. P. Feng, E. S. Tok, C. H. Sow, *ACS Appl. Mater. Interfaces* **2013**, *5*, 9594.
[40] H. Qiao, Z. Huang, X. Ren, S. Liu, Y. Zhang, X. Qi, H. Zhang, *Adv. Opt. Mater.* **2020**, *8*, 1900765.
[41] T. Dong, J. Simões, Z. Yang, *Adv. Mater. Interfaces* **2020**, *7*, 1901657.
[42] J. Jiang, X. Zou, Y. Lv, Y. Liu, W. Xu, Q. Tao, Y. Chai, L. Liao, *Nat. Commun.* **2020**, *11*, 4266.
[43] U. Khan, Y. T. Luo, L. Tang, C. J. Teng, J. M. Liu, B. L. Liu, H. M. Cheng, *Adv. Funct. Mater.* **2019**, *29*, 1807979.
[44] L. Q. Tu, R. R. Cao, X. D. Wang, Y. Chen, S. Q. Wu, F. Wang, Z. Wang, H. Shen, T. Lin, P. Zhou, X. J. Meng, W. D. Hu, Q. Liu, J. L. Wang, M. Liu, J. H. Chu, *Nat. Commun.* **2020**, *11*, 101.
[45] Y. J. Fang, A. Armin, P. Meredith, J. S. Huang, *Nat. Photonics* **2019**, *13*, 1.
[46] G. Konstantatos, *Nat. Commun.* **2018**, *9*, 5266.
[47] X. Zhou, L. Gan, W. M. Tian, Q. Zhang, S. Y. Jin, H. Q. Li, Y. Bando, D. Golberg, T. Y. Zhai, *Adv. Mater.* **2015**, *27*, 8035.

[48] C. F. Shen, Y. H. Liu, J. B. Wu, C. Xu, D. Z. Cui, Z. Li, Q. Z. Liu, Y. R. Li, Y. X. Wang, X. Cao, H. Kumazoe, F. Shimojo, A. Krishnamoorthy, R. K. Kalia, A. Nakano, P. D. Vashishta, M. R. Amer, A. N. Abbas, H. Wang, W. Z. Wu, C. W. Zhou, *ACS Nano* **2020**, *14*, 303.

[49] J. Li, Z. X. Wang, Y. Wen, J. W. Chu, L. Yin, R. Q. Cheng, L. Lei, P. He, C. Jiang, L. P. Feng, J. He, *Adv. Funct. Mater.* **2018**, *28*, 1706437.

[50] H. Xu, L. Hao, H. Liu, S. Dong, Y. Wu, Y. Liu, B. Cao, Z. Wang, C. Ling, S. Li, Z. Xu, Q. Xue, K. Yan, *ACS Appl. Mater. Interfaces* **2020**, *12*, 35250.